Enhanced Magnetoresistance under Bias Voltage in Fe/MgO/$MgAl_2O_4$/MgO/Fe Trilayer Tunneling Barrier Junction

Kenji Nawa,[1,2,*] Keisuke Masuda,[1] and Yoshio Miura[1,3]

[1] *Research Center for Magnetic and Spintronic Materials, National Institute for Materials Science (NIMS), 1-2-1 Sengen, Tsukuba 305-0047, Japan*

[2] *Graduate School of Engineering, Mie University, 1577 Kurima-machiya, Tsu 514-8507, Japan*

[3] *Center for Spintronics Research Network (CSRN), Graduate School of Engineering Science, Osaka University, 1-3 Machikaneyama, Toyonaka 560-8531, Japan*

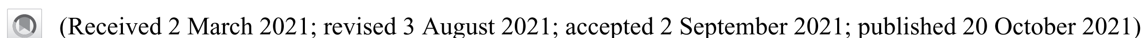

(Received 2 March 2021; revised 3 August 2021; accepted 2 September 2021; published 20 October 2021)

Experiments on magnetic tunnel junctions (MTJs) show that the use of a (001)-oriented spinel $MgAl_2O_4$ barrier improves the robustness of the tunneling magnetoresistance (TMR) ratio against bias voltage [Sukegawa *et al.*, Appl. Phys. Lett. 96, 212505 (2010)]; however, the maximum TMR ratio is very small compared with that of the MgO-based MTJ. To overcome this problem, we propose a MTJ with a trilayered tunnel-barrier junction, Fe/MgO/$MgAl_2O_4$/MgO/Fe, from first-principles calculations. The presence of the MgO interlayer between Fe and $MgAl_2O_4$ has the effect of enhancing the TMR ratio to more than 1000% at zero bias. The large TMR is maintained under a bias voltage. The results indicate the potential of a hybrid-type tunnel barrier that combines the advantages of MTJs containing a single MgO barrier (high TMR) and a single $MgAl_2O_4$ barrier (robustness to bias voltages). The MgO interlayer is found to play a key role in suppressing the transmittance of the minority-spin channel, and thus, the tunneling conductance of antiparallel magnetization is significantly reduced.

DOI: 10.1103/PhysRevApplied.16.044037

I. INTRODUCTION

Nonvolatile spin-based devices could potentially be exploited to realize a sustainable modern society, in which ultralow power consumption and ultrafast data-processing technologies are established by utilizing normally off memory architectures [1]. Magnetic tunnel junctions (MTJs), consisting of an insulating tunnel-barrier layer sandwiched between ferromagnetic (FM) electrodes, are the central device in practical spintronic applications, such as magnetoresistive random-access memories and magnetic sensors. A large tunnel magnetoresistance (TMR) ratio is required for high-performance devices. MTJs with highly crystalline MgO and bcc-based ferromagnets are theoretically demonstrated to have a large TMR ratio of more than 1000%. This originates from the coherent tunneling of highly spin-polarized electrons in the FM state, which are filtered by the so-called Δ_1-symmetric evanescent state in the MgO barrier [2–6], as predicted by pioneering theoretical studies [7,8]. Very recently, experiments succeeded in observing TMR ratios close to the theoretical prediction at low temperature, i.e., 914% (using Fe electrode) [9], 1144% (Co-Fe-B electrode) [5], and 2610% (Heusler Co_2(Mn,Fe)Si electrode) [10].

To enhance the output voltage of MTJ devices, it is essential to maintain a high TMR ratio, even upon application of a bias voltage. It is known that the TMR ratios of the MgO-based MTJs are significantly reduced upon applying a bias voltage. This is apparently the result of defects induced at the interface between the tunnel barrier and FM electrodes [11]. From a theoretical point of view, the TMR reduction occurs even in defect-free Fe/MgO/Fe MTJs [12,13]. The application of bias voltage causes the minority-spin Δ_1 band to increase the tunnel electrons in antiparallel magnetization; hence, the TMR ratio vanishes once a certain (relatively small) bias voltage is applied [2,4,14]. High-performance applications require a higher value of V_{half}, at which the TMR reduces to half of its zero-bias voltage.

The dependence of the TMR on the bias voltage is improved by using a MTJ with a spinel-type oxide tunnel barrier. The spinel oxides AB_2O_4 are advantageous in the rich structural and electronic properties, which can be optimized by selecting the constituent cations and their compositions. More recently, these oxides have been explored in terms of their capability of a tunnel barrier [13,15–25]. Among the spinel oxides, much attention is paid to $MgAl_2O_4$, owing to its very small lattice mismatch with Fe(001) ($\sim$0.3%). Experimentally, a large V_{half} ($\sim$1.0 V) is demonstrated in the fully epitaxially grown

*nawa.kenji@nims.go.jp

 © 2021 American Physical Society

Fe/$MgAl_2O_4$/Fe(001) MTJ structure [17]. In this MTJ, the Δ_1 state of the Fe electrodes couples with the $\tilde{\Delta}_1$ evanescent state of the $MgAl_2O_4$ barrier as in MgO MTJs. Moreover, due to different in-plane lattice periodicities between Fe(001) and $MgAl_2O_4$(001), a band-folding effect occurs in the two-dimensional Brillouin zone (BZ) of the in-plane wave vector in the Fe electrode. This induces additional conductive states that are folded at the zone boundary and couples to the $\tilde{\Delta}_1$ state at the Fe/$MgAl_2O_4$(001) interface [15]. A theoretical study reveals that the existence of the band-folding effect in the majority spins in Fe electrodes plays a role in improving the robustness of TMR against the bias voltages in an $MgAl_2O_4$ MTJ compared with the conventional MgO MTJ [13]. However, a theoretical TMR limit is very small compared with the MgO-based MTJs, owing to the sacrifice of the minority spins induced by the band-folding effect [15,24].

We aim to design tunnel-barrier materials for MTJs that maintain a high TMR ratio under bias application. In this study, we explore an $MgAl_2O_4$-based MTJ with an Fe(001) electrode, in which an MgO layer is inserted at the Fe/$MgAl_2O_4$ interface. Effects of MgO insertion on the TMR and its bias-voltage dependence are investigated using first-principles calculations. Our calculations demonstrate that a TMR ratio is significantly improved to more than 1000% at zero-bias voltage by inserting the MgO layer, and the TMR ratio remains high, even when the bias voltage is increased considerably. The underlying mechanism for the large TMR is attributed to a blocking of propagation of the minority-spin Δ_1 state in the inserted MgO layer because of the absence of the band-folding effect in the Fe/MgO interface. This phenomenon leads to a suppression of tunneling, especially in the minority-spin channel of Fe, thereby lowering the conductance for antiparallel magnetization. Our findings suggest the existence of a hybrid-type tunneling barrier that combines the benefits of MTJs with single MgO and single $MgAl_2O_4$ barriers. The proposed tunneling barrier has a high TMR and excellent bias-voltage dependence.

Herein, the *band-folding effect* is defined as follows. A folded band contributes to the conductance by coupling to an unfolded band at the junction of an electrode and a barrier with different in-plane lattice periodicities, as is seen in Fe/$MgAl_2O_4$(001) [15]. In the case of Fe/MgO(001), due to the same size of primitive cells for Fe(001) and MgO(001), a folded band of Fe in the doubled lattice never connects to an unfolded Δ_1 complex band of MgO [15]. Thus, Fe/MgO(001) does not show the band-folding effect.

We note that, although insertion of the MgO layer between the Fe and $MgAl_2O_4$ layers may be considered as overly artificial, our model is motivated by the fact that a bilayer consisting of MgO and $MgAl_2O_x$ is observed in a highly textured $MgAl_2O_4$(001) tunnel barrier after an annealing process, as referred to by the energy dispersive spectroscopy (EDS) analysis shown in Fig. 4(h) of Ref. [21]. This EDS line profile indicates the potential of employing the interlayer to modify the interface at the experimental level.

II. MODEL AND METHOD

As a model, we build a two-probe MTJ structure that consists of two semi-infinite Fe electrodes sandwiching an $MgAl_2O_4$ tunneling barrier of nine monolayers (MLs), in which MgO interlayers with one (1-ML), two (2-ML), or three (3-ML) MLs are inserted at the interfaces on both the left and the right (Fig. 1). The thickness of nine MLs corresponds to one unit cell of the $MgAl_2O_4$ spinel. Our total-energy calculations determine that the most stable atomic structure at the MgO/$MgAl_2O_4$ interface is a hollow-site structure with respect to the O atoms between MgO and $MgAl_2O_4$ (see Appendix for details), while the Fe/MgO interface stabilizes the on-top alignment of Fe and O of the MgO layer. The in-plane lattice constant is fixed to that of double-bcc Fe ($a = 2a_{\mathrm{Fe}} = 5.73$ Å), which corresponds to almost 45° rotation of the $MgAl_2O_4$ unit cell ($a_{\mathrm{MgAl_2O_4}} = a_{0,\mathrm{MgAl_2O_4}}/\sqrt{2}$ with a cubic lattice constant of $MgAl_2O_4$, $a_{0,\mathrm{MgAl_2O_4}} = 8.08$ Å). It is worth knowing that, at the Fe/MgO interface, many misfit dislocations are induced, owing to lattice mismatch between Fe and MgO ($\sim 3\%$, where $a_{\mathrm{MgO}} = a_{0,\mathrm{MgO}}/\sqrt{2}$ with a cubic lattice constant of MgO, $a_{0,\mathrm{MgO}} = 4.21$ Å), but we assume the in-plane lattice constant to be matched to Fe, although structural distortion along the c axis is taken into account to relax the MgO structure, as we have done previously [22,24,26]. We refer to this model as the MgO-inserted MTJ, whereas the system without the inserted MgO layer, which is calculated for reference purposes, is referred to as the pristine model.

Density-functional theory calculations are performed on the basis of the nonequilibrium Green's function method implemented in the Quantum Atomistix ToolKit (Quantum-ATK) [27]. A norm-conserving pseudopotential method and generalized gradient approximation (GGA) exchange-correlation functional are employed [28], and a

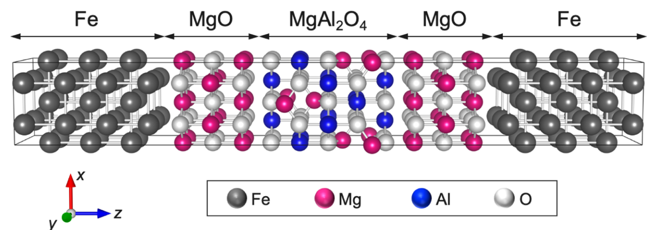

FIG. 1. Geometry of the Fe/MgO/$MgAl_2O_4$/MgO/Fe MTJ with the 3-ML MgO interlayer inserted at the Fe/$MgAl_2O_4$ interface (scattering region) as an example. Balls represent Fe (gray), Mg (magenta), Al (blue), and O (white).

linear combination of atomic orbitals (LCAO) formalism with the single-ζ-polarized basis set is adopted to describe the wave functions. The BZ is sampled with a Monkhorst-Pack k-point mesh of an 11×11 grid along the (k_x, k_y) plane and a 101 grid along the perpendicular k_z direction. A dense k_z mesh is required to accurately evaluate the chemical potential of the scattering region shown in Fig. 1 and ensure that it corresponds with that of the Fe electrode. The real-space-density mesh cutoff for describing the electrostatic potential and electron density is set to 80 htr. Self-consistent field (SCF) calculations are continued until the total energy converges to the criterion of 10^{-4} htr.

Atoms in the four MLs of Fe at both ends are fixed to the bulk geometry, whereas all other atoms are fully relaxed by force calculations with a relaxation-force criterion of 0.05 eV/Å. After relaxation, the interfacial distances of the Fe/MgO and MgO/$MgAl_2O_4$ interfaces are found to be 2.19 and 2.17 Å, respectively (see Appendix for calculation details).

The electrical current, $I^{\sigma}(V)$, can be calculated from the Landauer-Bütticker formula:

$$I^{\sigma}(V) = \frac{e}{h}\int T^{\sigma}(E, V)\,[f_L(\mu_L) - f_R(\mu_R)]\,dE, \tag{1}$$

where $T^{\sigma}(E, V)$ is the transmittance of tunnel electrons with spin channel σ (σ is $\uparrow$ or $\downarrow$) at energy E, and $f_L(\mu_L)$ and $f_R(\mu_R)$ represent the Fermi-Dirac distribution functions, $f(\mu) = 1/[e^{\beta(E-\mu)} + 1]$, for the Fe electrodes on the left and the right ($\beta = 1/k_B T$). Here, e is the (positive) elementary charge, h is Planck's constant, k_B is the Boltzmann constant, and T is the electron temperature. The TMR ratio in the optimistic definition is then obtained as TMR (%) $= (I_{\rm P} - I_{\rm AP})/I_{\rm AP} \times 100$, where $I_{\rm P}$ and $I_{\rm AP}$ are the electric currents summed over spins σ in the parallel (P) and antiparallel (AP) magnetizations, respectively. A 75×75 k-point mesh on the k_x-k_y plane in the BZ is confirmed to be sufficient for evaluating the transmittance without numerical errors. A finite bias voltage, V, is applied to the electrodes by shifting the chemical potential to satisfy the definition of $\mu_L - \mu_R = -eV$. The electrical current flows from the left electrode to the right when a positive bias voltage is applied, i.e., the tunneling electrons flow from the right electrode to the left, and vice versa when the bias voltage is negative. Thus, the chemical-potential shifts for the electrodes on the left and the right are given as $\mu_L = E_F - \text{eV}/2$ and $\mu_R = E_F + \text{eV}/2$, respectively, for positive bias ($\mu_R = \mu_L$ at zero bias).

Practically, as electrodes, Fe bulk systems given by $2 \times 2 \times 1$ supercells (periodic along the transport direction k_z) are additionally attached to the left and right sides of the structure shown in Fig. 1, referred to as the (nonperiodic) scattering region, to treat the incident electrons coming from the electrode. The electronic structures of the Fe electrodes are first obtained. Then, the nonequilibrium electronic structure in the scattering region is determined by SCF procedures with boundary conditions where the scattering wave functions and their derivatives are matched to the Bloch-wave functions of the electrodes, at which the chemical potentials are shifted according to the applied bias voltages. More details are available in Ref. [27].

III. RESULTS AND DISCUSSION

A. At zero-bias voltage

At zero-bias voltage, we obtain a TMR of 1884% by inserting a 1-ML MgO interlayer at the Fe/$MgAl_2O_4$ interface. This value is 1 order of magnitude greater than that of the pristine MTJ (TMR = 125%). Large TMR values are also obtained for models with thicker MgO layers: 1154 and 3967% for 2- and 3-ML MgO-inserted MTJs, respectively, as summarized in Table I. This study does not reveal a clear dependence of the TMR ratio on the number of MLs up to 3-ML MgO insertions. However, the fact that the highest TMR ratio is obtained with the highest number of MgO interlayers suggests that the TMR may become higher if the number of MgO layers is further increased. Here, however, we present the results of the model with a 1-ML MgO interlayer, because this structure confirms the explicit effect of MgO insertion.

The transmittance spectra in $\mathbf{k}_{\parallel}$ space are shown in Fig. 2. For P magnetization, the majority-spin state has a simple transmittance shape with a peak at the Γ point [Fig. 2(a)]. The highest value of transmittance originates from the Δ_1-symmetric bands (s, p_z, and d_{z^2} orbitals), in accordance with previous calculations reported for both single-barrier MgO and $MgAl_2O_4$ MTJs [7,8,15]. The minority-spin states give rise to sharp peaks, but no Γ-centered peak appears [Fig. 2(b)]. This tendency is different from that of the pristine $MgAl_2O_4$ MTJ, where the folded Δ_1 bands induce finite transmittance at Γ [15]. This is reflected in the transmittance of AP magnetization, leading to zero transmittance at Γ [Fig. 2(c)]. The difference in the TMR ratios between the MgO-inserted and pristine MTJs is well characterized by transmittance at the Γ point, as guaranteed numerically by a discussion based on the calculated conductance at Γ (see Ref. [29]). Therefore, we

TABLE I. TMR ratios at zero-bias voltage for MgO-inserted MTJs with MgO interlayers comprising 1-, 2-, and 3-MLs inserted at the Fe/$MgAl_2O_4$ interface (number of MgO layers is shown in parentheses in the second column). The result for the pristine MTJ is also shown.

		TMR (%)
MgO-inserted	Fe/MgO(1)/$MgAl_2O_4$/MgO(1)/Fe	1884
	Fe/MgO(2)/$MgAl_2O_4$/MgO(2)/Fe	1154
	Fe/MgO(3)/$MgAl_2O_4$/MgO(3)/Fe	3967
Pristine	Fe/$MgAl_2O_4$/Fe	125

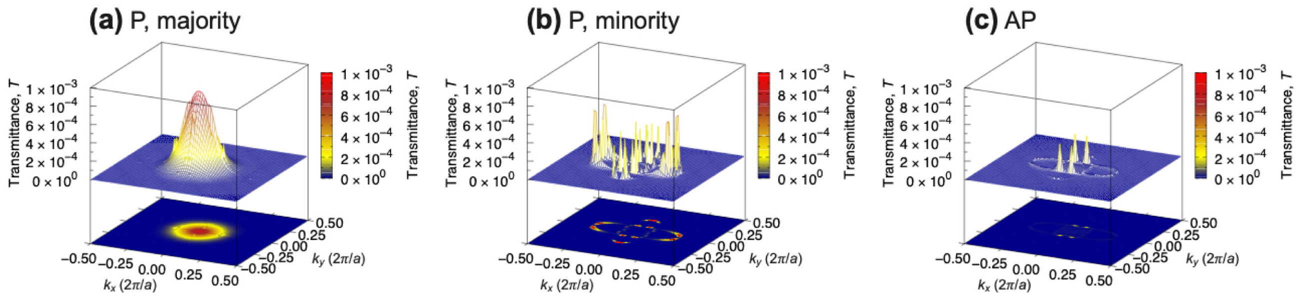

FIG. 2. Transmittance spectra for $\mathbf{k}_{\parallel}$ space in the MgO-inserted MTJ for (a) majority- and (b) minority-spin states of P magnetization and (c) AP magnetization.

focus on Γ to discuss the effect of the MgO interlayer on the transport properties hereafter.

Figure 3(a) shows the energy-dependent transmittance, $T(E)$, at Γ for the MgO-inserted MTJ. $T(E)$ for the majority spin of P magnetization increases logarithmically from −2.2 to 3 eV. A steplike transmittance profile can be observed in the minority-spin channel of P magnetization in the energy region of −0.9 to 0.1 eV [see filled area in Fig. 3(a)], which also results in $T(E)$ having a similar shape for AP magnetization. The pristine model shown in Fig. 3(b) has transport profiles similar to those of the MgO-inserted MTJ. However, in the energy region −0.9 to 0.1 eV, the relative difference between the majority-spin $T(E)$ in P magnetization and others is significant in the MgO-inserted MTJ, in contrast with that in the pristine MTJ. Possible behaviors of tunnel electrons for each model at the Fermi level are illustrated schematically in Figs. 3(c) and 3(d). The tunnel electrons are blocked inside a specific barrier region, depending on the spin channel and magnetization state in the MgO-inserted MTJ, whereas, in the pristine case, all electrons can pass through the $MgAl_2O_4$ tunnel barrier, which we discuss next.

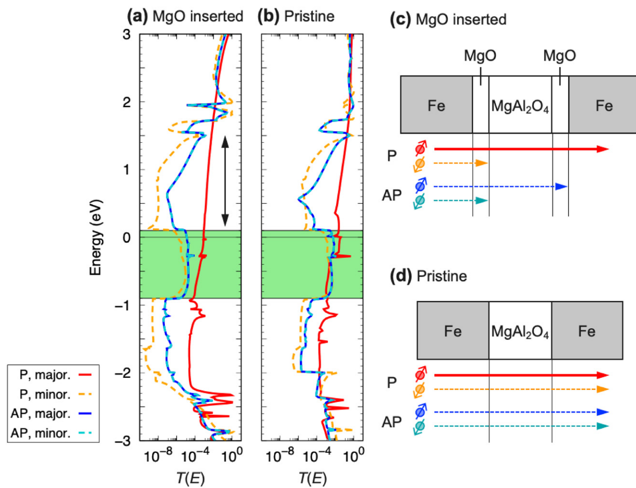

FIG. 3. Transmittance profiles as a function of energy, $T(E)$, at Γ for (a) MgO-inserted and (b) pristine MTJs. Red (solid) and orange (dashed) lines represent the majority- and minority-spin states for P, and blue (solid) and sky-blue (dashed) lines represent the majority- and minority-spin states for AP. Filled area (−0.9 to 0.1 eV) corresponds to the energy region in which steplike $T(E)$ profiles exist for P (minority spin) and AP (majority and minority spins). (For the AP state, the spin channels and majority- and minority-spin states are defined for electrons incident from the left Fe electrode; i.e., the former refers to the tunnel from the *majority* spin of the left electrode to the minority spin of the right electrode, whereas the latter refers to the tunnel from the *minority* spin of the left electrode to the majority spin of the right electrode.) Illustrations of tunnel processes at the Fermi level for (c) MgO-inserted and (d) pristine MTJs. Solid arrows indicate dominant tunneling, while dashed arrows indicate blocked tunneling in a specific barrier region or less dominant tunneling.

Basically, an interpretation of the tunnel-electron phenomena can be addressed from the electronic band structures of the insulating tunnel barrier and FM electrodes in their bulk states [7,8], and we discuss here the origin of TMR in the same way. Since the in-plane lattice periodicity of $MgAl_2O_4$ is greater than those of MgO and Fe by a factor of 2, $a_{MgAl_2O_4} \approx 2a_{MgO}$ and $a_{MgAl_2O_4} \approx 2a_{Fe}$, the BZ of $MgAl_2O_4$ [$BZ_{MgAl_2O_4}$ in Fig. 4(a)] shrinks along the in-plane direction compared with those of a 1 × 1 cell of MgO and Fe [$BZ_{MgO,1}$ and $BZ_{Fe,1}$ in Figs. 4(b) and 4(c)]. However, in the MTJ structure, the tunnel electrons can be considered to go through the BZ corresponding to $BZ_{MgAl_2O_4}$, which is smallest in the MTJ, thereby the BZ of MgO also shrinks to $BZ_{MgO,2}$, given by the 2 × 2 supercell, and the same is true for Fe ($BZ_{Fe,2}$). This phenomenon is illustrated in Figs. 4(a)–4(c), where part of the electronic states of $BZ_{MgO,1}$ ($BZ_{Fe,1}$), referring to the states outside $BZ_{MgO,2}$ ($BZ_{Fe,2}$), are folded at zone boundaries of $BZ_{MgO,2}$ ($BZ_{Fe,2}$). More specifically, the bands along Γ'–Z' are folded onto the Γ–Z path [see dashed and solid arrows in Figs. 4(b) and 4(c)].

The complex band structure for $MgAl_2O_4$ presents the $\tilde{\Delta}_1$ evanescent state within the energy band gap, the complex wave vector of which is $\kappa_{MgAl_2O_4} = \mathrm{Im}(k_z) = 0.30\ (2\pi/c)$ at the Fermi level [Fig. 4(d)]. For the MgO band structure, two of the Δ_1 evanescent states can be seen: one arises from the original band structure in $BZ_{MgO,1}$

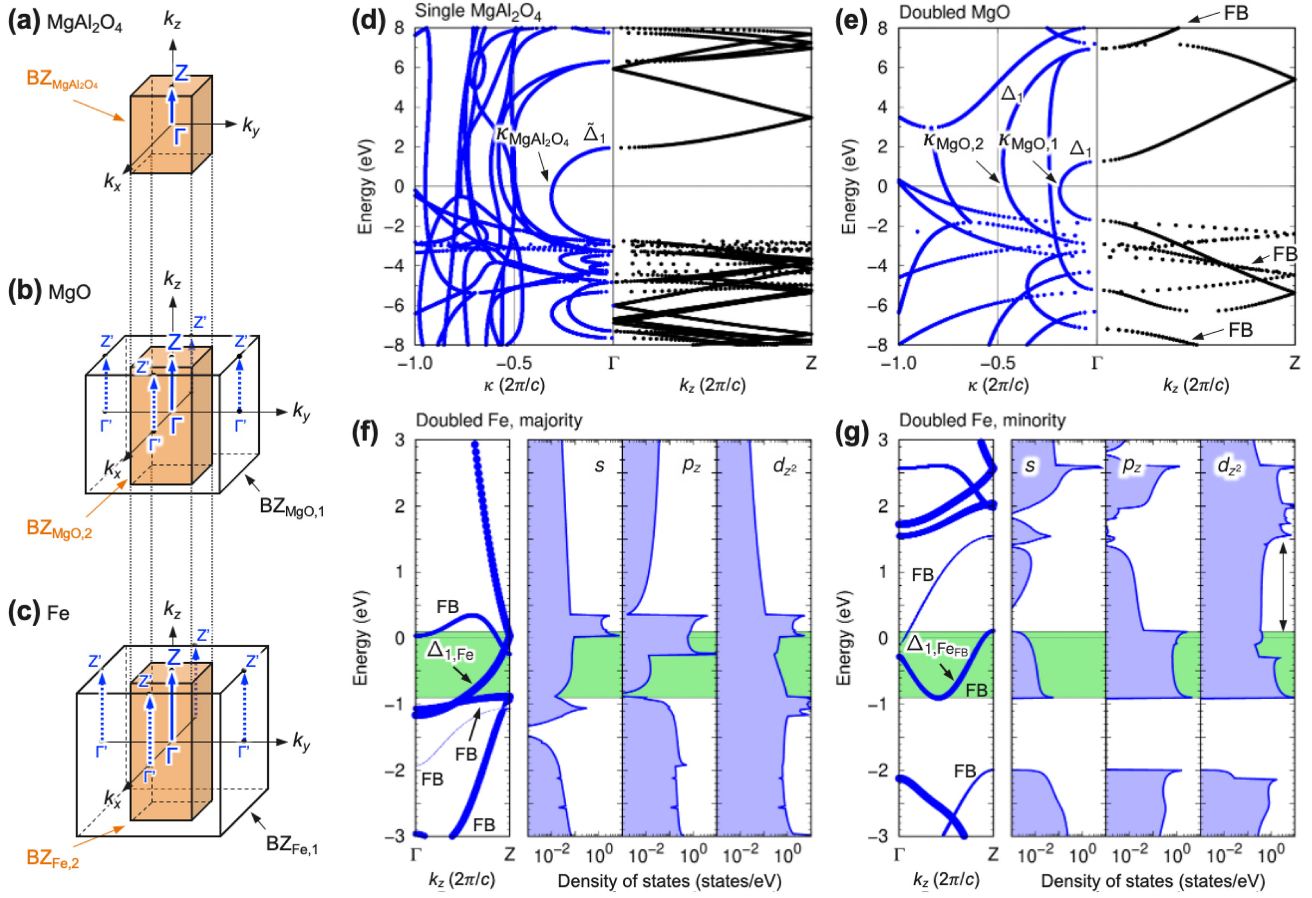

FIG. 4. Illustrations of BZs and band-folding effect for (a) $MgAl_2O_4$, (b) MgO, and (c) Fe in bulk states (see text). Band structures along the conductive direction ($\Gamma \rightarrow Z$) for (d) $MgAl_2O_4$ given by 1×1 cell and (e) MgO given by 2×2 supercell, where right panel shows real part of k_z and left panel shows imaginary part of it, i.e., decay rate κ. Electronic structures for Fe, 2×2 supercell, projected on the Δ_1 state for (f) majority- and (g) minority-spin states. Left panel shows the band structure along Γ–Z path [Z corresponds to $(0, 0, 1/2)$] and right panel shows the corresponding DOS projections onto s, p_z, and d_{z^2} orbitals. Fermi energy is set to zero. In (e)–(g), label FB indicates bands being folded from $\Gamma' \rightarrow Z'$ path, and those of $\Delta_{1,\mathrm{Fe}}$ and $\Delta_{1,\mathrm{Fe_{FB}}}$ are explained in the text.

with $\kappa_{\mathrm{MgO},1} = 0.19$ $(2\pi/c)$, while the other arises from the folded-band (FB) structures in $\mathrm{BZ_{MgO,2}}$ with $\kappa_{\mathrm{MgO},2} = 0.46$ $(2\pi/c)$ [30]. Similarly, several Δ_1-symmetric FBs appear in the Fe band structure. For the majority-spin state, one of the FBs is crossing the Fermi level and the remaining bands are found at around -3 to -1 eV [left panel in Fig. 4(f)]. The minority-spin state shows the FBs crossing the Fermi level, indicating the broken half metallicity of the Δ_1 state, and one FB at -2 eV below the Fermi level [left panel in Fig. 4(g)]. Taking into account the discussion of the steplike $T(E)$ in Figs. 3(a) and 3(b), we identify bands marked with ($\Delta_{1,\mathrm{Fe}}$) and ($\Delta_{1,\mathrm{Fe_{FB}}}$) as important states for understanding the characteristic $T(E)$ behavior (corresponding to the energy region of -0.9 to 0.1 eV, shown by the filled area in related figures).

As reported previously [15], the folded Δ_1 band of the doubled Fe lattice ($\Delta_{1,\mathrm{Fe_{FB}}}$) is explicitly distinguished from the unfolded band of the single unit cell ($\Delta_{1,\mathrm{Fe}}$). The unfolded Fe band never connects with the folded evanescent state of MgO, and the same is true between the folded band of Fe and the unfolded band of MgO. In the P state of the MgO-inserted model, since the majority-spin state is the unfolded state, $\Delta_{1,\mathrm{Fe}}$, the electrons incident from the left Fe electrode pass through the tunnel barrier by connecting with three evanescent states: $\kappa_{\mathrm{MgO},1}$ in the left MgO, $\kappa_{\mathrm{MgAl_2O_4}}$ in the central $MgAl_2O_4$, and $\kappa_{\mathrm{MgO},1}$ in the right MgO; $\Delta_{1,\mathrm{Fe}} \rightarrow \kappa_{\mathrm{MgO},1} \rightarrow \kappa_{\mathrm{MgAl_2O_4}} \rightarrow \kappa_{\mathrm{MgO},1} \rightarrow \Delta_{1,\mathrm{Fe}}$. In contrast, in the minority-spin state of P, since the band at the Fermi level is folded, $\Delta_{1,\mathrm{Fe_{FB}}}$, the electrons pass through as $\Delta_{1,\mathrm{Fe_{FB}}} \rightarrow \kappa_{\mathrm{MgO},2} \rightarrow \kappa_{\mathrm{MgAl_2O_4}} \rightarrow \kappa_{\mathrm{MgO},2} \rightarrow \Delta_{1,\mathrm{Fe_{FB}}}$. Here, we can discuss qualitatively the decay rate of tunnel electrons in each barrier region by employing complex wave vectors of their evanescent states. Since $\kappa_{\mathrm{MgO},2}$ is clearly greater than $\kappa_{\mathrm{MgO},1}$ and $\kappa_{\mathrm{MgAl_2O_4}}$ [Figs. 3(d) and 3(e)], the wave function of the tunnel electron connected to $\kappa_{\mathrm{MgO},2}$ decays very rapidly. Therefore, the tunnel of the minority-spin state may be suppressed and its transmittance becomes small,

unlike the majority-spin state, as illustrated in Fig. 3(c). In this manner, the tunnel process for the AP state can be understood as follows. The majority-spin electrons tunnel by the $\Delta_{1,\mathrm{Fe}} \to \kappa_{\mathrm{MgO},1} \to \kappa_{\mathrm{MgAl_2O_4}} \to \kappa_{\mathrm{MgO},2} \to \Delta_{1,\mathrm{FeFB}}$ process, and the minority-spin electrons tunnel by the $\Delta_{1,\mathrm{FeFB}} \to \kappa_{\mathrm{MgO},2} \to \kappa_{\mathrm{MgAl_2O_4}} \to \kappa_{\mathrm{MgO},1} \to \Delta_{1,\mathrm{Fe}}$ process, resulting in the majority spin being blocked by the right MgO interlayer and the minority spin being blocked by the left MgO interlayer [Fig. 3(c)]. On the other hand, in the pristine model, all of the spin channels can pass through the $MgAl_2O_4$ barrier by connecting with $\kappa_{\mathrm{MgAl_2O_4}}$, regardless of P and AP states, although the majority spins in the P state provide a major contribution to transmittance [13,15,24], as shown in Fig. 3(d). It may also be worth mentioning that, in the well-known Fe/MgO/Fe MTJ, the Δ_1-symmetric electrons can travel through the MgO barrier via the $\kappa_{\mathrm{MgO},1}$ evanescent state only for majority-spin P state, which gives a giant TMR ratio [7,8].

Based on our discussion, it may be possible to suppress TMR reduction originating from the band-folding effect, especially in the AP state for MTJs with $MgAl_2O_4$ barriers, by modifying the interfacial structure. We emphasize that the insertion of the MgO interlayer thickens the tunnel barrier, so that the absolute value of $T(E)$ becomes smaller overall [Figs. 3(a) and 3(b)]. However, the decrease in the AP state is more obvious than that in the P state (we focus only on the majority spins for simplicity), which thus indicates that the TMR ratio in the MgO-inserted MTJ is governed by the effects of the MgO interlayer.

Although the d_{z^2} orbital has a large DOS for the majority- and minority-spin states over a wide energy region [right panels in Figs. 4(f) and 4(g)], the s and p_z orbitals mainly contribute to the tunnel electrons, but the d_{z^2} contribution is rather minor. To discuss this, we focus here on the minority-spin tunnel process in P magnetization. In Fig. 4(g), the $\Delta_{1,\mathrm{FeFB}}$ band has components of s, p_z, and d_{z^2} states, but only the first two of these have similar DOS shapes that increase rapidly in the energy range of -0.9 to 0.1 eV, which is similar to the steplike shape of $T(E)$ [orange (dashed) line in Figs. 3(a) and 3(b)]. The DOS of d_{z^2} has a large value (but not a simple steplike shape) in the same energy region, and it is so over a wide region above the Fermi level, for example, in the range indicated by the arrow (0.1–1.5 eV) in Fig. 4(g). However, the magnitude of $T(E)$ is very small in the range of 0.1–1.5 eV [see arrow in Fig. 3(a)], indicating that d_{z^2} may not contribute so much. Therefore, our results are consistent with the well-known fact that tunnel conductance is dominated by the sp electrons, with their small effective masses, and the d electrons are negligible [31].

B. Under finite bias voltage

The dependences of the TMR ratios of the MgO-inserted and pristine MTJs on the finite bias voltage are compared in Fig. 5. Our calculations reproduce previous results on

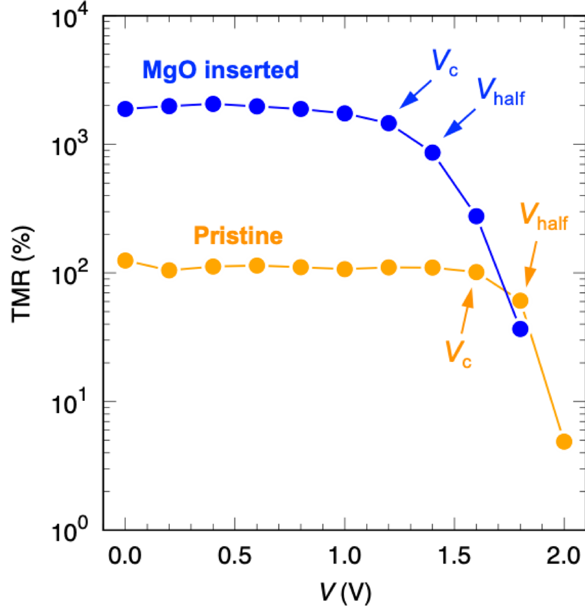

FIG. 5. TMR ratios as a function of applied bias voltage for MgO-inserted (blue) and pristine (orange) MTJs. Arrows indicate V_c and V_{half} for each MTJ model.

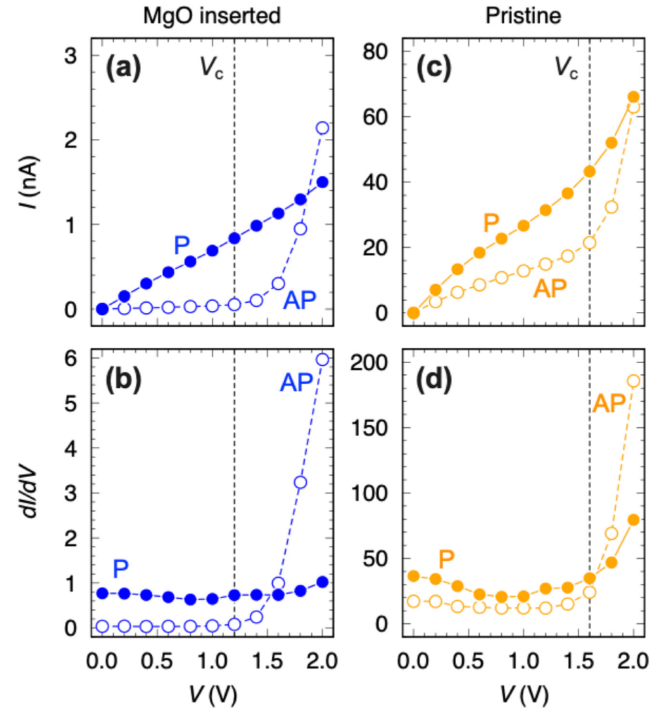

FIG. 6. (a) I–V and (b) dI/dV curves for the MgO-inserted MTJ. (c),(d) Same as (a),(b) for the pristine MTJ. Solid (open) circles represent P (AP) magnetization. Vertical dashed line indicates V_c for each model.

the pristine $MgAl_2O_4$ MTJ [13], where the TMR ratio is almost constant at 100–120% at a lower V, and then decreases at the critical bias voltage, $V_c = 1.6$ V. Here, we define V_c as the bias voltage at which the TMR begins to decrease [32]. Furthermore, V_{half} is evaluated to be 1.8 V (TMR = 61%) [33]. In the MgO-inserted model, the TMR ratio continues to remain in excess of 1000% at a lower V, which is very similar to the tendency of the pristine model, except for the TMR ratio. The values of V_c and V_{half} are found to be 1.2 and 1.4 V (TMR = 862%), respectively. A direct comparison between these models based on V_c and V_{half} (and the TMR ratio at the bias voltage) may not be meaningful because of their different barrier thicknesses. However, our calculations demonstrate successfully that a relatively large value of $V_{\mathrm{half}}(= 1.4$ eV) is obtained by inserting the MgO layer.

The improvement upon MgO insertion is also clear from the current–voltage (I–V) and dI/dV curves in Fig. 6. In the MgO-inserted model, the current, I, for P magnetization monotonically increases as V increases, which results in a constant dI/dV value [solid circles in Figs. 6(a) and 6(b)]. The upward tendency in I is similar to that of the pristine MTJ [solid circles in Figs. 6(c) and 6(d)]. Importantly, for AP magnetization, the I–V and dI/dV curves change significantly as a result of MgO insertion. The value of I is very small below V_c in the MgO-inserted MTJ, with the value of dI/dV approaching zero [open circles in Figs. 6(a) and 6(b)]; in contrast, for the pristine MTJ, a finite slope of I is even obtained below V_c [open circles in Figs. 6(c) and 6(d)]. Our results confirm that the value of I (and dI/dV) for AP magnetization in the MTJ with a single MgO barrier is almost zero at low V (results are not shown), which is consistent with published results [13], that is, the tendency is similar to that of the MgO-inserted MTJ. From these discussions, we conclude that the MgO-inserted MTJ model, to a certain extent, resembles the $MgAl_2O_4$-based MTJ for P magnetization and the MgO-based MTJ for AP magnetization, suggesting a hybrid-type tunneling barrier for the MTJ.

Finally, we discuss the mechanism underlying the relatively high V_{half} in the MgO-inserted MTJ. Figure 7 presents the effect of the applied bias voltage on $T(E)$. The fundamental $T(E)$ profiles at zero-bias voltage are presented in Fig. 3(a), and we use these as the starting point to discuss changes of $T(E)$ as a consequence of the effect of V. For the case of the P state, the majority-spin $T(E)$ shifts to higher energy when V is applied, but it always increases logarithmically inside the bias window (red line in Fig. 7), leading to a monotonic increase in current, I, in Fig. 6(a). This $T(E)$ profile for the majority-spin state is crucial for improving V_{half} and originates from the Δ_1 FBs in the majority-spin state of the Fe electrode found in the lower-energy region (−3 to −0.9 eV) at zero-bias voltage [Fig. 3(a)], as previously reported [13]. Notably, in the Fe/MgO/Fe MTJ, $T(E)$ for the P state rapidly decreases in this energy region because of the absence of FBs [13]. The minority-spin $T(E)$ is no longer predominant and has become negligible (orange line in Fig. 7).

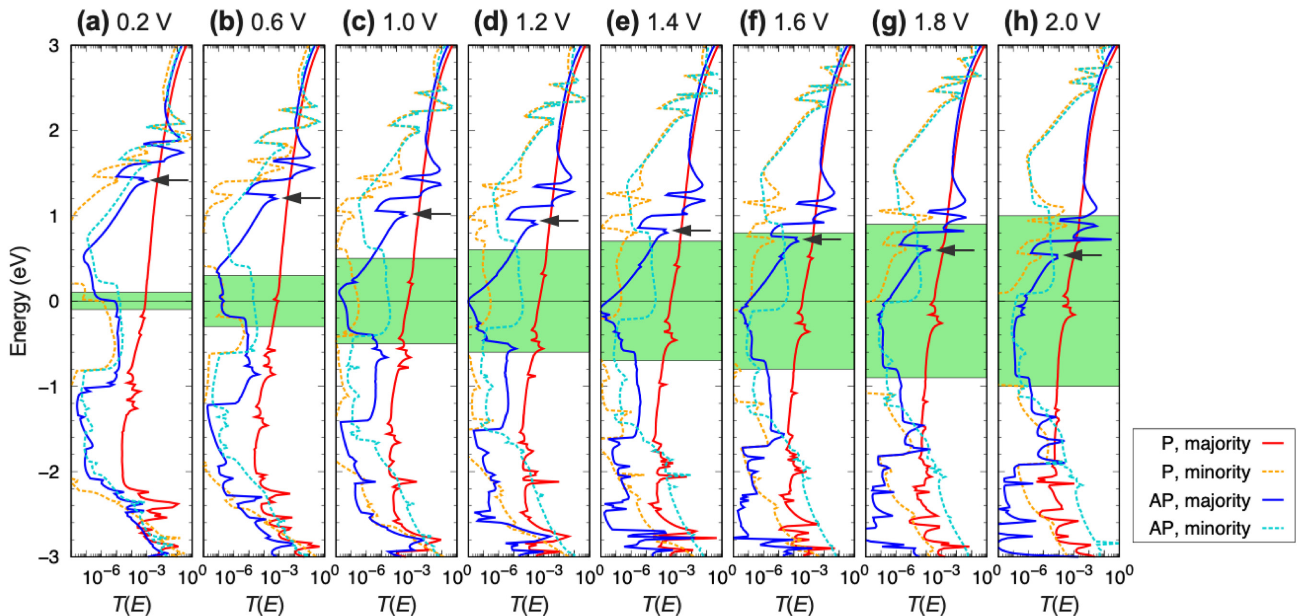

FIG. 7. Transmittance profile as a function of energy calculated at Γ under finite bias voltage for the MgO-inserted MTJ: (a) $V = 0.2$, (b) 0.6, (c) 1.0, (d) 1.2, (e) 1.4, (f) 1.6, (g) 1.8, and (h) 2.0 V. Energy region to be integrated in Eq. (1) is shown as the filled area, referred to as the bias window. Arrows indicate the peak $T(E)$ of the minority-spin state in the AP state (see text). V_c corresponds to (d) $V_{\mathrm{bias}} = 1.2$ V. Notation is the same as in Figs. 3(a) and 3(b).

The reduction in the TMR is characterized by AP magnetization, in which $T(E)$ for the majority- and minority-spin states moves in opposite directions energetically. Specifically, the former moves to higher energy and the latter moves to lower energy (blue and sky-blue lines in Fig. 7). We find that the contribution to I becomes dominant in the minority-spin state rather than in the majority-spin state at high V. Indeed, the majority-spin $T(E)$ continues to exhibit a steplike shape inside the bias window, and its contribution to I for the AP state remains constant. In contrast, in the minority state, because the peak $T(E)$ (see arrows in Fig. 7) gradually enters the bias window as a larger V is applied, the integrated $T(E)$ value becomes dominant after $V_c = 1.2$ V. Then, the TMR eventually becomes zero at $V = 1.8$–2.0 V.

Notably, since the folded bands of Fe in the majority-spin states lead to the robustness of TMR against bias voltage, the highly crystalline structure of $MgAl_2O_4$ is essential for the excellent bias dependence in the MgO-inserted MTJ. If the in-plane lattice constant of $MgAl_2O_4$ is halved, for example, by the introduction of cation-site disordering [23,34], the folded bands no longer appear in the Fe electrode and the TMR obtained might be sensitive to bias voltages, which is the case for the MgO MTJ [13]. Highly crystalline $MgAl_2O_4$, with a doubled in-plane lattice compared with that of Fe (and MgO), may be accessible by fine control of the oxidation conditions [16,35]. In particular, the two-step process of repeated Mg–Al alloy deposition and postoxidation proposed recently [35] may lead to the potential to fabricate well-ordered $MgAl_2O_4$ in the MTJ. The formation of the oxidized FM layer between the electrode and insulator and vacancies of O in the insulator also lead to a lowering of the TMR, even at zero-bias voltage [36–41]; thus, defect-free heterointerfaces are important for both high TMR and excellent bias dependence.

IV. SUMMARY

We insert an MgO layer into $Fe/MgAl_2O_4/Fe$ and investigate the effect of this modification of the interface on the TMR and its dependence on the bias voltage of the resulting $Fe/MgO/MgAl_2O_4/MgO/Fe$ MTJ by means of first-principles calculations. The TMR ratio is enhanced to more than 1000% by inserting the MgO layer, and a large TMR ratio is maintained under finite bias voltage. The MgO interlayer plays a key role in blocking Δ_1-state propagations in the minority-spin states of the Fe electrode, such that the tunnel conductance of the AP magnetization state is reduced. This mechanism allows us to propose a hybrid-type tunneling barrier that exhibits the advantages of both a single MgO MTJ (high TMR) and a single $MgAl_2O_4$ MTJ (robustness to bias voltages) simultaneously.

ACKNOWLEDGMENTS

The authors are grateful to H. Sukegawa and S. Mitani at NIMS and S. Ichikawa, T. Suzuki, K. Nakada, and T. Sasaki at TDK Corporation for fruitful discussions and critical suggestions. This work is supported, in part, by TDK Corporation; Grants-in-Aid for Scientific Research (Grants No. JP16H06332, No. JP17H06152, No. JP20H02190, and No. JP20K14782) from the Japan Society for the Promotion of Science; the Tatematsu Foundation; and the Data-Science Research Center for Material, Quantum, and Measurement Technologies, Mie University. Computations are performed using the facilities of the Numerical Materials Simulator at NIMS.

APPENDIX: STABILITY OF INTERFACIAL STRUCTURE

The stability of the interfaces of the Fe/MgO and $Fe/MgAl_2O_4$ structures are clarified by *ab-initio* calculations, which show that the O atom of the insulating oxide is stabilized in the on-top configuration of Fe with strong chemical bonding between the O p_z and Fe d_{z^2} orbitals. However, it is not clear which is the most stable structure after insertion of the MgO layer at the $Fe/MgAl_2O_4$ interface. Thus, the stability of the structure of the $MgO/MgAl_2O_4$ interface is determined by conducting a total-energy analysis from first principles.

We consider four possible surface structures in total, as shown in Fig. 8. For the first model, the O atom of MgO is located at the hollow site with respect to the O atoms of the $MgAl_2O_4$ surface [referred to as the hollow site; see Fig. 8(a)]. The second model has the O atom of MgO aligned with the O atom of $MgAl_2O_4$ [on-top site; Fig. 8(b)]. For the two remaining models, the O atom of MgO is located at the bridge site with respect to the O atoms of $MgAl_2O_4$, but they are distinguished from each other by nonequivalent sites, depending on the cation (Al)

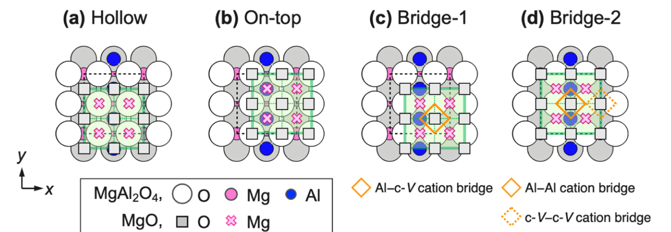

FIG. 8. Top views of four models of MgO on the $MgAl_2O_4$ surface: (a) hollow, (b) on-top, (c) bridge-1, and (d) bridge-2 configurations. Large (white), medium (magenta), and small (blue) circles represent O, Mg, and Al, respectively, for $MgAl_2O_4$; square (gray) and cross (light magenta) marks represent O and Mg, respectively, for MgO. Solid diamond (orange) in (c) shows the O anions of MgO at the cation-bridge site of Al–c-V, and the solid and dashed diamonds in (d) show O at the cation-bridge sites of Al–Al and c-V–c-V (see the text for details).

distribution at the $MgAl_2O_4$ surface. In the third model, the O atom of MgO is positioned at the cation-bridge site between Al and c-V (Al–c-V), where c-V represents the cation-vacancy site at the $MgAl_2O_4$ interface [bridge-1 site; Fig. 8(c)]. Finally, the fourth model has the O of MgO positioned at the cation-bridge sites of Al–Al and c-V–c-V [bridge-2 site; Fig. 8(d)].

The ground states of these models are obtained using the following procedures. First, the interfacial distance between MgO and $MgAl_2O_4$, $d_{MgO/MgAl_2O_4}$, is optimized. The total energies are calculated by varying $d_{MgO/MgAl_2O_4}$ from geometrically relaxed atomic structures, where the initial distance between Fe and MgO, $d_{Fe/MgO}$, is assumed to be 2.20 Å [13], and the lowest-energy point is searched. Here, a $7 \times 7 \times 1$ k-point grid is used. Second, with $d_{MgO/MgAl_2O_4}$ optimized in the first step and the reported value of $d_{Fe/MgO} (= 2.20$ Å), the ground-state atomic structure is obtained from the relaxation with a denser $11 \times 11 \times 1$ k-point grid, after which the total energy of the ground state is evaluated. First-principles calculations are performed using the ultrasoft pseudopotentials [42,43] within the GGA [28].

Table II summarizes the calculated interfacial distances and total energies. The values of $d_{Fe/MgO}$ are almost the same for these models and are slightly smaller than that in the Fe/MgO/Fe MTJ (2.20 Å) [13], whereas $d_{MgO/MgAl_2O_4}$ changes depending on the $MgO/MgAl_2O_4$ interfaces. The interfacial structures are reconstructed, as shown in Fig. 9. Structural changes in the inserted MgO layer are significant, whereas the $MgAl_2O_4$ layers hardly change. A comparison of the total energies indicates that the hollow-site configuration between the O atoms of the MgO and $MgAl_2O_4$ layers is the most stable structure, followed by the bridge-1 (relative energy difference of 2.49 eV), bridge-2 (2.97 eV), and on-top (3.95 eV) configurations.

The stability determined from the energetics can be understood from the fact that the O anions prefer to distribute in such a way to lower electrostatic repulsions at the interface. Accordingly, the on-top configuration becomes unstable, where the O anions of MgO and $MgAl_2O_4$ directly interact with each other by σ-like (p_z–p_z) hybridization, resulting in the longest value of $d_{MgO/MgAl_2O_4} = 2.97$ Å. The bridge-1 model is more preferable in terms of its energy than that of the bridge-2 model, with an energy difference of 0.48 eV. The origin of this can be understood by focusing on the *cation* (Mg) site of MgO on the $MgAl_2O_4$ surface. The Mg site of MgO in the bridge-1 model corresponds to the cation-bridge sites of Al–Al and c-V–c-V [Fig. 8(c)]. Consequently, at the MgO layer, only Mg at the c-V–c-V cation-bridge site shifts significantly along the z direction, as shown in Fig. 9(c). This might be because the Mg cations tend to satisfy the charge-neutrality condition with the O anions of the $MgAl_2O_4$ surface for stabilization. On the other hand, in the bridge-2 model, all Mg atoms of the MgO layer are equivalent, with respect to the $MgAl_2O_4$ surface, and are located at the cation-bridge site of Al–c-V, where no significant displacement can be seen in Fig. 9(d).

TABLE II. Optimized interfacial distances for Fe/MgO ($d_{Fe/MgO}$) and $MgO/MgAl_2O_4$ ($d_{MgO/MgAl_2O_4}$) in units of Å and relative total energies, E_{total}, in eV per interface for different O alignments at the $MgO/MgAl_2O_4$ interface (see also Fig. 8). $d_{Fe/MgO}$ and $d_{MgO/MgAl_2O_4}$ are determined from average values of the z positions of the atoms in each layer after relaxation of the atomic geometry (see also Fig. 9).

	Interfacial distance (Å)		
	$d_{Fe/MgO}$	$d_{MgO/MgAl_2O_4}$	E_{total} (eV)
Hollow	2.19	2.17	0.00
On-top	2.15	2.97	3.95
Bridge-1	2.16	2.51	2.49
Bridge-2	2.17	2.65	2.97

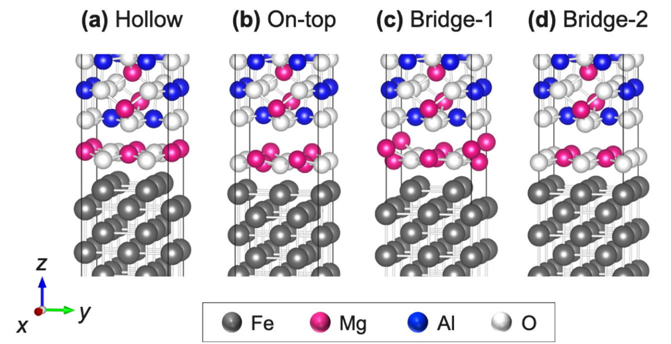

FIG. 9. Relaxed interfacial structures of $Fe/MgO/MgAl_2O_4$, where O of MgO is located at the (a) hollow, (b) on-top, (c) bridge-1, and (d) bridge-2 sites. Atoms are represented by balls in different colors, as shown in Fig. 1.

[1] F. Hellman *et al.*, Interface-induced phenomena in magnetism, Rev. Mod. Phys. **89**, 025006 (2017), and references therein.

[2] S. Yuasa, T. Nagahama, A. Fukushima, Y. Suzuki, and K. Ando, Giant room-temperature magnetoresistance in single-crystal Fe/MgO/Fe magnetic tunnel junctions, Nat. Mater. **3**, 868 (2004).

[3] S. S. P. Parkin, C. Kaiser, A. Panchula, P. M. Rice, B. Hughes, M. Samant, and S.-H. Yang, Giant tunnelling magnetoresistance at room temperature with MgO (100) tunnel barriers, Nat. Mater. **3**, 862 (2004).

[4] D. D. Djayaprawira, K. Tsunekawa, M. Nagai, H. Maehara, S. Yamagata, N. Watanabe, S. Yuasa, Y. Suzuki, and K. Ando, 230% room-temperature magnetoresistance in CoFeB/MgO/CoFeB magnetic tunnel junctions, Appl. Phys. Lett. **86**, 092502 (2005).

[5] S. Ikeda, J. Hayakawa, Y. Ashizawa, Y. Lee, K. Miura, H. Hasegawa, M. Tsunoda, F. Matsukura, and H. Ono, Tunnel magnetoresistance of 604% at 300K by suppression of Ta diffusion in CoFeB/MgO/CoFeB pseudo-spin-valves annealed at high temperature, Appl. Phys. Lett. **93**, 082508 (2008).

[6] S. Yuasa, A. Fukushima, H. Kubota, Y. Suzuki, and K. Ando, Giant tunneling magnetoresistance up to 410% at room temperature in fully epitaxial Co/MgO/Co magnetic tunnel junctions with bcc Co(001) electrodes, Appl. Phys. Lett. **89**, 042505 (2006).

[7] W. H. Butler, X.-G. Zhang, T. C. Shulthess, and J. M. MacLaren, Spin-dependent tunneling conductance of Fe|MgO|Fe sandwiches, Phys. Rev. B **63**, 054416 (2001).

[8] J. Mathon and A. Umerski, Theory of tunneling magnetoresistance of an epitaxial Fe/MgO/Fe(001) junction, Phys. Rev. B **63**, 220403(R) (2001).

[9] T. Scheike, Q. Xiang, Z. Wen, H. Sukegawa, T. Ohkubo, K. Hono, and S. Mitani, Exceeding 400% tunnel magnetoresistance at room temperature in epitaxial Fe/MgO/Fe(001) spin-valve-type magnetic tunnel junctions, Appl. Phys. Lett. **118**, 042411 (2021).

[10] K. Moges, Y. Honda, H.-X. Liu, T. Uemura, M. Yamamoto, Y. Miura, and M. Shirai, Enhanced half-metallicity of off-stoichiometric quaternary heusler alloy Co_2(Mn, Fe)si investigated through saturation magnetization and tunneling magnetoresistance, Phys. Rev. B **93**, 134403 (2016).

[11] H. J. M. Swagten, Handbook of Magnetic Materials (edited by K. H. J. Buschow; Elsevier Science, Amsterdam) **17** (2008).

[12] I. Rungger, O. Mryasov, and S. Sanvito, Resonant electronic states and $I-V$ curves of Fe/MgO/Fe(100) tunnel junctions, Phys. Rev. B **79**, 094414 (2009).

[13] K. Masuda and Y. Miura, Bias voltage effects on tunneling magnetoresistance in Fe/$MgAl_2O_4$/Fe(001) junctions: Comparative study with Fe/MgO/Fe(001) junctions, Phys. Rev. B **96**, 054428 (2017).

[14] W. Wang, H. Sukegawa, R. Shan, S. Mitani, and K. Inomata, Giant tunneling magnetoresistance up to 330% at room temperature in sputter deposited Co_2FeAl/MgO/CoFe magnetic tunnel junctions, Appl. Phys. Lett. **95**, 182505 (2009).

[15] Y. Miura, S. Muramoto, K. Abe, and M. Shirai, First-principles study of tunneling magnetoresistance in Fe/$MgAl_2O_4$/Fe(001) magnetic tunnel junctions, Phys. Rev. B **86**, 024426 (2012).

[16] H. Sukegawa, K. Inomata, and S. Mitani, Post-oxidized Mg-Al-O(001) coherent tunneling barrier in a wide range of resistance-area products, Appl. Phys. Lett. **105**, 092403 (2014).

[17] H. Sukegawa, H. Xiu, T. Ohkubo, T. Furubayashi, T. Niizeki, W. Wang, S. Kasai, S. Mitani, K. Inomata, and K. Hono, Tunnel magnetoresistance with improved bias voltage dependence in lattice-matched Fe/spinel $MgAl_2O_4$/Fe(001) junctions, Appl. Phys. Lett. **96**, 212505 (2010).

[18] M. Belmoubarik, H. Sukegawa, T. Ohkubo, S. Mitani, and K. Hono, Effect of Mg-Al insertion on magnetotransport properties in epitaxial Fe/sputter-deposited $MgAl_2O_4$/Fe(001) magnetic tunnel junctions, AIP Adv. **7**, 055908 (2017).

[19] H. Sukegawa, S. Mitani, T. Ohkubo, K. Inomata, and K. Hono, Low-resistive monocrystalline Mg-Al-O barrier magnetic tunnel junctions for spin-transfer magnetization switching, Appl. Phys. Lett. **103**, 142409 (2013).

[20] M. Belmoubarik, H. Sukegawa, T. Ohkubo, S. Mitani, and K. Hono, $MgAl_2O_4$(001) based magnetic tunnel junctions made by direct sputtering of a sintered spinel target, Appl. Phys. Lett. **108**, 132404 (2016).

[21] Ikhtiar, H. Sukegawa, X. Xu, M. Belmoubarik, H. Lee, S. Kasai, and K. Hono, Giant tunnel magnetoresistance in polycrystalline magnetic tunnel junctions with highly textured $MgAl_2O_4$(001) based barriers, Appl. Phys. Lett. **112**, 022408 (2018).

[22] K. Masuda and Y. Miura, Perpendicular magnetic anisotropy at the Fe/$MgAl_2O_4$ interface: Comparative first-principles study with Fe/MgO, Phys. Rev. B **98**, 224421 (2018).

[23] S. Ju, Y. Miura, K. Yamamoto, K. Masuda, K. i. Uchida, and J. Shiomi, Machine learning analysis of tunnel magnetoresistance of magnetic tunnel junctions with disordered $MgAl_2O_4$, Phys. Rev. Res. **2**, 023187 (2020).

[24] K. Nawa, K. Masuda, and Y. Miura, Interfacial resonant tunneling induced by folded bands and providing highly spin-polarized current in spinel-oxide barrier junctions, Phys. Rev. B **102**, 144423 (2020).

[25] T. Scheike, H. Sukegawa, T. Ohkubo, K. Hono, and S. Mitani, Comparative study of spin-dependent transport in Co_2FeAl/$MgAl_2O_4$/CoFe magnetic tunnel junctions with and without thin CoFe interface insertion: An elastic and inelastic scattering model analysis, J. Phys. D: Appl. Phys. **53**, 045001 (2020).

[26] K. Yamamoto, K. Masuda, K.-I. Uchida, and Y. Miura, Strain-induced enhancement of the seebeck effect in magnetic tunneling junctions via interface resonant tunneling: Ab initio study, Phys. Rev. B **101**, 094430 (2020).

[27] S. Smidstrup *et al.*, QuantumATK: An integrated platform of electronic and atomic-scale modelling tools, J. Phys.: Condens. Matter **32**, 015901 (2020).

[28] J. P. Perdew, K. Burke, and M. Ernzehof, Generalized gradient approximation made simple, Phys. Rev. B **77**, 3865 (1996).

[29] Here, we define the conductance ratio of P to AP at Γ as G_P^Γ/G_{AP}^Γ, where G_P^Γ and G_{AP}^Γ are the sums of transmittance in the majority- and minority-spin states for P and AP magnetizations, respectively. The value of G_P^Γ/G_{AP}^Γ is 67.3 for the MgO-inserted MTJ, whereas it is 6.6 for the pristine model; the scale factor of the latter is approximately one tenth of the former. Indeed, this difference is consistent with the comparison of G_P/G_{AP} (G_P and G_{AP} are the conductances of P and AP magnetizations summed over the entire $\mathbf{k}_\parallel$ space), where $G_P/G_{AP} = 19.9$ and 2.3 for the systems with and without MgO-layer insertion, respectively; the scaling factor of these values varies by approximately one ninth.

[30] Note that the value of the complex wave vector depends on the basis set in our calculations. When the double-ζ-polarized basis set is used for the LCAO formalism, the κ values for each band result in $\kappa_{MgAl_2O_4} = 0.36$, $\kappa_{MgO,1} = 0.30$, and $\kappa_{MgO,2} = 0.73(2\pi/c)$. This indicates that the decay rate of $MgAl_2O_4$ is comparable to that of (unfolded) MgO, $\kappa_{MgAl_2O_4} \approx \kappa_{MgO,1}$, consistent with the plane-wave

basis calculations, about $0.5(2\pi/c)$ [15,44], although a discrepancy in the absolute value remains between different methods. The κ values presented in the text, which are obtained from the single-ζ-polarized basis set, show the non-negligible difference between $\kappa_{\mathrm{MgAl_2O_4}}$ and $\kappa_{\mathrm{MgO,1}}$. However, the decay rate of the folded band, $\kappa_{\mathrm{MgO,2}}$, is much larger; more specifically, $\kappa_{\mathrm{MgO,2}}$ is larger than $\kappa_{\mathrm{MgO,1}}$ by a factor of 2.4, as in the double-ζ-polarized results. Therefore, we discuss our results based on the single-ζ-polarized results; this is appropriate for consistency throughout the paper, since all transport properties are calculated by the single-ζ basis set.

[31] G.-F. Li, Y. Honda, H.-X. Liu, K. Masuda, M. Arita, T. Uemura, M. Yamamoto, Y. Miura, M. Shirai, T. Saito, F. Shi, and P. M. Voyles, Effect of nonstoichiometry on the half-metallic character of Co_2MnSi investigated through saturation magnetization and tunneling magnetoresistance ratio, Phys. Rev. B **89**, 014428 (2014).

[32] More strictly, V_c is defined as the bias voltage at which dI/dV begins to increase.

[33] Because the dependence of the finite bias voltage is investigated in increments of 0.2 V in this study, the values of V_c and V_{half} may not be evaluated quantitatively. However, we assume that V_c and V_{half} are useful for a qualitative comparison between the MgO-inserted and pristine MTJ models.

[34] H. Sukegawa, Y. Miura, S. Muramoto, S. Mitani, T. Niizeki, T. Ohkubo, K. Abe, M. Shirai, K. Inomata, and K. Hono, Enhanced tunnel magnetoresistance in a spinel oxide barrier with cation-site disorder, Phys. Rev. B **86**, 184401 (2012).

[35] S. Ichikawa, P.-H. Cheng, H. Sukegawa, T. Ohkubo, K. Hono, S. Mitani, and K. Nakada, Controlling oxygen distribution of an $MgAl_2O_4$ barrier for magnetic tunnel junctions by two-step process, Appl. Phys. Lett. **117**, 122409 (2020).

[36] E. Y. Tsymbal and D. G. Pettifor, Spin-polarized electron tunneling across a disordered insulator, Phys. Rev. B **58**, 432 (1998).

[37] X.-G. Zhang, W. H. Butler, and A. Bandyopadhyay, Effects of the iron-oxide layer in Fe-FeO-MgO-Fe tunneling junctions, Phys. Rev. B **68**, 092402 (2003).

[38] H. Itoh, J. Ozeki, and J. Inoue, Effects of disorder on tunnel magnetoresistance in Fe/MgO/Fe junctions, J. Magn. Magn. Mater. **303**, e205 (2006).

[39] G. X. Du, S. G. Wang, Q. L. Ma, Y. Wang, R. C. C. Ward, X.-G. Zhang, C. Wang, A. Kohn, and X. F. Han, Spin-dependent tunneling spectroscopy for interface characterization of epitaxial Fe/MgO/Fe magnetic tunnel junctions, Phys. Rev. B **81**, 064438 (2010).

[40] A. T. Hindmarch, K. J. Dempsey, D. Ciudad, E. Negusse, D. A. Arena, and C. H. Marrows, Fe diffusion, oxidation, and reduction at the CoFeB/MgO interface studied by soft *x*-ray absorption spectroscopy and magnetic circular dichroism, Appl. Phys. Lett. **96**, 092501 (2010).

[41] J. P. Velev, K. D. Belashchenko, S. S. Jaswal, and E. Y. Tsymbal, Effect of oxygen vacancies on spin-dependent tunneling in Fe/MgO/Fe magnetic tunnel junctions, Appl. Phys. Lett. **90**, 072502 (2007).

[42] G. Kresse and J. Furthmuüller, Efficient iterative schemes for ab initio total-energy calculations using a plane-wave basis set, Phys. Rev. B **54**, 11169 (1996).

[43] G. Kresse and D. Jourbert, From ultrasoft pseudopotentials to the projector augmented-wave method, Phys. Rev. B **59**, 1758 (1999).

[44] J. Zhang, X.-G. Zhang, and X. F. Han, Spinel oxides: Δ_1 spin-filter barrier for a class of magnetic tunnel junctions, Appl. Phys. Lett. **100**, 222401 (2012).